

See discussions, stats, and author profiles for this publication at: <https://www.researchgate.net/publication/274643838>

Efficient Directional Excitation of Surface Plasmons by a Single-Element Nanoantenna

ARTICLE *in* NANO LETTERS · APRIL 2015

Impact Factor: 13.59 · DOI: 10.1021/acs.nanolett.5b00181 · Source: PubMed

READS

69

7 AUTHORS, INCLUDING:



Wenjie Yao

Peking University

3 PUBLICATIONS 0 CITATIONS

[SEE PROFILE](#)



Zhi Li

Peking University

45 PUBLICATIONS 624 CITATIONS

[SEE PROFILE](#)



Chengwei Sun

Peking University

12 PUBLICATIONS 20 CITATIONS

[SEE PROFILE](#)



Jianjun Chen

Peking University

39 PUBLICATIONS 468 CITATIONS

[SEE PROFILE](#)

¹ Efficient Directional Excitation of Surface Plasmons by a Single-Element Nanoantenna

³ Wenjie Yao,^{§,†} Shang Liu,^{§,†} Huimin Liao,^{*,†} Zhi Li,^{*,†} Chengwei Sun,^{†,‡} Jianjun Chen,^{†,‡}
⁴ and Qihuang Gong^{†,‡}

⁵ [†]School of Physics, Peking University, Beijing 100871, China

⁶ [‡]State Key Laboratory for Mesoscopic Physics, Peking University, Beijing 100871, China

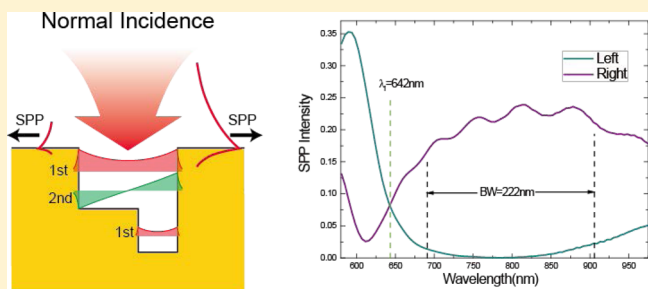
⁷ Supporting Information

ABSTRACT: Directional light scattering is important in basic research and real applications. This area has been successfully downscaled to wavelength and subwavelength scales with the development of optical antennas, especially single-element nanoantennas. Here, by adding an auxiliary resonant structure to a single-element plasmonic nanoantenna, we show that the highly efficient lowest-order antenna mode can be effectively transferred into inactive higher-order modes. On the basis of this mode conversion, scattered optical fields can be well manipulated by utilizing the interference between different antenna modes. Both broadband directional excitation of surface plasmon polaritons (SPPs) and inversion of SPP launching direction at different wavelengths are experimentally demonstrated as typical examples. The proposed strategy based on mode conversion and mode interference provides new opportunities for the design of nanoscale optical devices, especially directional nanoantennas.

KEYWORDS: *nanoantenna, surface plasmon polaritons, directional scattering, mode conversion, single-element*

²³ **L**ight field manipulation is a basic subject in optics and has
²⁴ several important applications. With the development of
²⁵ nano-optics, this area has been downscaled to nanoscales
²⁶ accompanied by several important progresses.^{1–3} Typical
²⁷ nanoscale devices, such as nanowaveguides,⁴ nanoantennas,^{5–7}
²⁸ and nanolasers^{8,9} have been proposed and demonstrated.
²⁹ Among these devices, nanoantennas are important because of
³⁰ their ability to control the absorption and radiation of light at
³¹ nanoscale dimensions. Especially, proper designs of nano-
³² antennas provide efficient means to control the directionality of
³³ scattered optical fields.^{6,7} This phenomenon is highly desired in
³⁴ many applications, including communications, solar cells, and
³⁵ sensors, among others.

³⁶ Optical nanoantennas could be analogously designed with
³⁷ classical microwave antennas to achieve directional light
³⁸ scattering. By carefully regulating the scattering amplitudes,
³⁹ phases, and spatial separations of a series of antenna elements,
⁴⁰ multielement antennas, such as the Yagi–Uda configuration,^{6,7}
⁴¹ have been proposed to control absorption and emission
⁴² directions based on constructive and destructive interferences
⁴³ in different directions. However, these multielement antennas
⁴⁴ are relatively large in size and complex to fabricate. To
⁴⁵ overcome these deficiencies, single-element nanoantennas have
⁴⁶ been proposed to obtain strong directional scattering.^{10–14}
⁴⁷ Instead of using the interference between different antenna
⁴⁸ elements in a multielement antenna, a single-element nano-
⁴⁹ antenna utilizes interference between different optical modes of
⁵⁰ an antenna. Unfortunately, higher-order optical modes



generally cannot be excited as efficiently as the lowest mode⁵¹ by external optical fields because strong field gradients on the⁵² nanoscales are required to match the complex modal fields of⁵³ higher-order modes. Consequently, structures of either single-⁵⁴ element antennas^{12,13} or external excitation fields¹⁴ must be⁵⁵ well designed and controlled; thus, increased complexities in⁵⁶ sample fabrications or experiments are expected.⁵⁷

In this study, we explore a novel degree of freedom to⁵⁸ effectively excite higher-order antenna modes, which is through⁵⁹ mode conversion. Mode conversion has been utilized to excite⁶⁰ dark modes in plasmonic structures.^{15,16} However, the⁶¹ conversion efficiencies are generally quite limited because the⁶² conversions are conducted by nonresonant structures. Here, by⁶³ adding an auxiliary resonant structure to the main structure of a⁶⁴ single-element nanoantenna, we show that the energy of the⁶⁵ highly efficient lowest-order antenna mode can be effectively⁶⁶ transferred into higher-order modes with the aid of the⁶⁷ participation of the optical mode in the auxiliary structure. This⁶⁸ phenomenon greatly facilitates further manipulations of⁶⁹ scattered optical fields by exploiting the interference between⁷⁰ different antenna modes. As a proof of principle, we⁷¹ demonstrate a single-element nanoantenna for efficient direc-⁷² tional excitation of surface plasmon polaritons (SPPs)^{17–24} by⁷³

Received: January 16, 2015

Revised: March 21, 2015

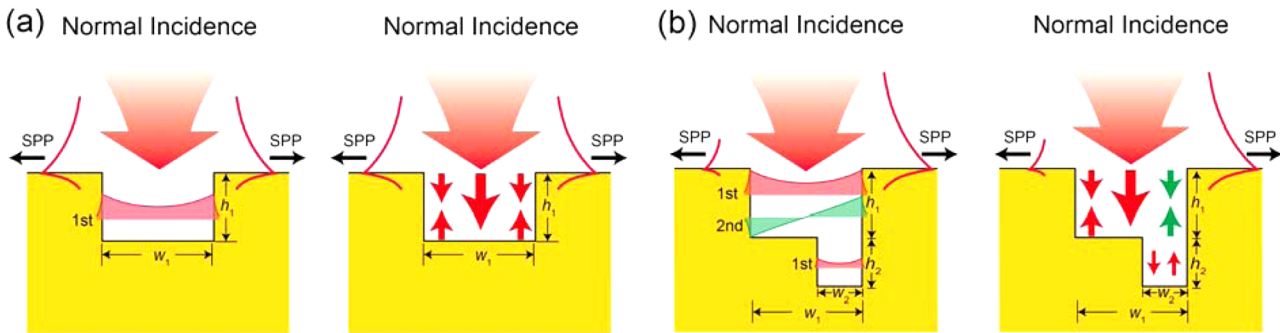


Figure 1. Schematic diagrams of SPP excitations by a single-element plasmonic nanoantenna without and with an auxiliary structure. The left panels in (a) and (b) show the modal field distributions of different waveguide modes in the metallic grooves, whereas the right panels indicate corresponding mode propagating processes (red and green arrows represent the first and second modes, respectively). (a) At normal incidence, only the symmetric first mode in the subwavelength groove without an auxiliary structure can be excited because of excitation symmetry. This causes equal SPP launching intensities to the left and right directions. (b) The energy of the active first mode in the main groove can be effectively transferred into the energy of the inactive second mode when a small auxiliary nanogroove is added to the bottom of the main groove. This phenomenon enables the antenna to further manipulate scattered optical fields (for instance, to obtain directional SPP excitation) through the interference between the symmetric first and antisymmetric second modes.

utilizing the mode conversion between an active first-order and
inertial second-order mode in a subwavelength metallic groove.
Inversion of SPP launching direction at different wavelengths is
also observed, which is attributed to the contribution of a
nonpropagating (i.e., below cut off) third-order mode. The
proposed method based on mode conversion and mode
interference provides new opportunities for the design of
nanoscale optical devices, especially in the research area of
directional nanoantennas.

The sample structure considered in this study is a
subwavelength groove on a metal surface, which could be
regarded as an efficient plasmonic antenna.^{25,26} SPPs can be
launched with high efficiency when the structure is illuminated
by a normal incident beam. However, only the symmetric first-
order (first) waveguide mode in the subwavelength metallic
groove is active because of excitation symmetry in normal
incidence. This feature causes equal SPP launching intensities
to the left and right directions, as schematically shown in Figure
1a. To obtain directional SPP excitation, the antisymmetric first-
order (second) waveguide mode in the groove must
become active (for detailed information concerning different
waveguide modes in the metallic grooves, see Section 1 in the
Supporting Information). Although this occurrence can be
achieved via oblique incidence,^{27,28} low absolute efficiency
becomes a drawback because an excitation beam cannot be
tightly focused in oblique incidence. This study explores a novel
degree of freedom to efficiently excite the antisymmetric
second mode through mode conversion. This is realized by
adding a small auxiliary nanogroove to the bottom of the main
groove, as schematically shown in Figure 1b. The symmetric
first waveguide mode in the main groove is excited with high
efficiency when a normal incident beam is tightly focused to the
entrance of the upper main groove. This waveguide mode
propagates downward and excites the first waveguide mode in
the lower auxiliary nanogroove which then gets highly reflected
at the metallic groove bottom. The first waveguide mode in the
auxiliary nanogroove exhibits strong field gradients on the
nanoscale and partly overlaps with the antisymmetric second
mode in the main groove (see the left figure in Figure 1b).
Therefore, the reflected first mode in the auxiliary nanogroove
can effectively excite and activate the second mode in the upper
main groove; consequently, the energy of the active first mode

in the main groove can be successfully converted into the
energy of the inactive second mode, with the aid of the auxiliary
structure. This phenomenon enables the antenna to further
manipulate scattered optical fields (for instance, to obtain
directional SPP excitation) through the interference between
the symmetric first and antisymmetric second modes. The
above mechanism of mode conversion and mode interference
can be theoretically described by a semianalytical model, which
is provided in detail in Section 2 in the Supporting Information,
and calculation results by this model quantitatively agree with
the direct simulation results. It is also noted that, although the
proposed antenna structure in Figure 1b looks similar to the
previously reported asymmetric slit structures (e.g., in
Reference 18), the underlying physical mechanism is completely
different (for detailed comparison between the two structures,
see Section 3 in the Supporting Information).

We perform numerical simulations using finite element
method (FEM) by COMSOL Multiphysics to verify the above
idea of mode conversion. The permittivity of gold as a function
of wavelength is taken from a previous literature,²⁹ and the
value is expanded using the method of interpolation. The
incident wavelength is initially set to $\lambda = 800$ nm. For
simplicity, the width of the auxiliary nanogroove is fixed to $w_2 = 200$ nm ($\sim 0.25\lambda$) so that only the first waveguide mode exists
in the auxiliary nanogroove. The width of the main groove is set
to $w_1 = 550$ nm ($\sim 0.7\lambda$), which ensures that only the first and
second waveguide modes are propagating modes in the main
groove. When downward propagating, the first or second
waveguide mode in the upper main groove encounters the
lower auxiliary nanogroove, they are partly reflected and partly
transferred into each other (see the right-side inset in Figure 2).
The mode-conversion behavior can be quantitatively described
by a reflection matrix R , with the matrix element R_{ij} ($i,j = 1,2$)
denoting the conversion coefficient from the downward j th
mode to the upward i th mode and $|R_{ij}|^2$ representing the power
flow of the upward i th mode when the incident power flow of
the downward j th mode is normalized to be unity at the bottom
of the main groove. Figure 2 shows the calculated amplitudes of
the four matrix elements ($|R_{ij}|$) at various depths h_2 of the
auxiliary nanogroove. These coefficients are extracted from the
total electromagnetic field by using mode orthogonality^{30,31}
between different waveguide modes in waveguide theories.^{30,31}

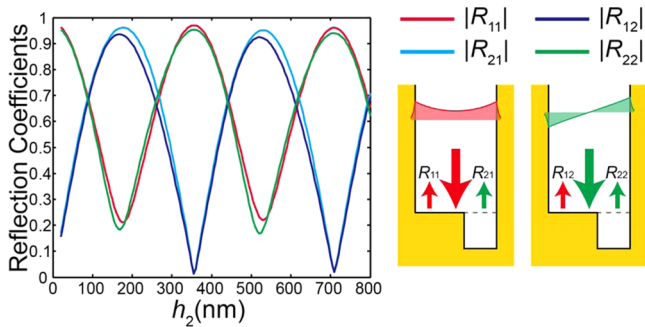


Figure 2. Efficient mode conversion in a single-element plasmonic nanoantenna with the auxiliary structure. The left panel shows calculated amplitudes of the four elements of the reflection matrix \mathbf{R} at various depths h_2 of the auxiliary nanogroove (incident wavelength $\lambda = 800$ nm, groove widths $w_1 = 550$ nm and $w_2 = 200$ nm). The right-side inset provides a schematic explanation to the four matrix elements.

The cross-conversion coefficients between the two modes ($|R_{12}|$ and $|R_{21}|$) vary from 0 to 0.95, which can be well controlled through h_2 . This means that up to 90% of the power of incident mode can be transferred into the power of the other mode. Therefore, mode conversion provides a highly efficient means of exciting the inactive second mode in the single-element antenna, considering that the symmetric first mode can be excited by normal incident beam with very high efficiency.^{25,26} Meanwhile, this method exhibits the advantage of having no critical requirement on external excitation fields and only weakly increases the complexity of sample fabrication.

Because higher-order antenna modes in a single-element nanoantenna can be effectively excited through mode conversion, further manipulation of scattered optical fields

becomes convenient. For instance, we demonstrate directional excitation of SPPs,^{17–24} which is highly desired in many plasmonic applications. Figure 3a schematically shows the three main origins of the final SPPs on the front metal surface excited by the proposed antenna structure in Figure 1b. These origins include the SPPs excited by the directly incident beam and the upward propagating first and second modes at the entrance of the upper main groove. The SPPs launched to the left and right directions are in phase for the first two origins (indicated by two cross-in-circle symbols on the left and right sides), but in antiphase in the antisymmetric second mode excitation (indicated by a dot in circle symbol on the left side and a cross in circle on the right side). This implies that the three SPP components may just cancel each other in one direction and interfere constructively in the other direction under proper conditions. Thus, a highly efficient directional excitation of SPPs is obtained.

The specific condition can be achieved by adjusting the depths h_1 and h_2 of the main and auxiliary grooves because amplitudes of the upward first and second modes can be primarily controlled by h_2 through mode conversion, whereas the phase difference between the two modes can be adjusted by h_1 . Figure 3b shows the simulated SPP intensities (quantified by SPP power flows normalized by the incident power flow on the groove entrance) that are launched to the left and right directions at various h_1 and h_2 . Each peak of the leftward SPP intensity approximately corresponds to a trough in the rightward SPPs, and vice versa. Thus, by choosing proper groove depths, highly directional SPP excitations can be achieved in both the left and right directions (for details, see Figures S10 and S11 in the Supporting Information). For comparison, the previously reported asymmetric slits enable

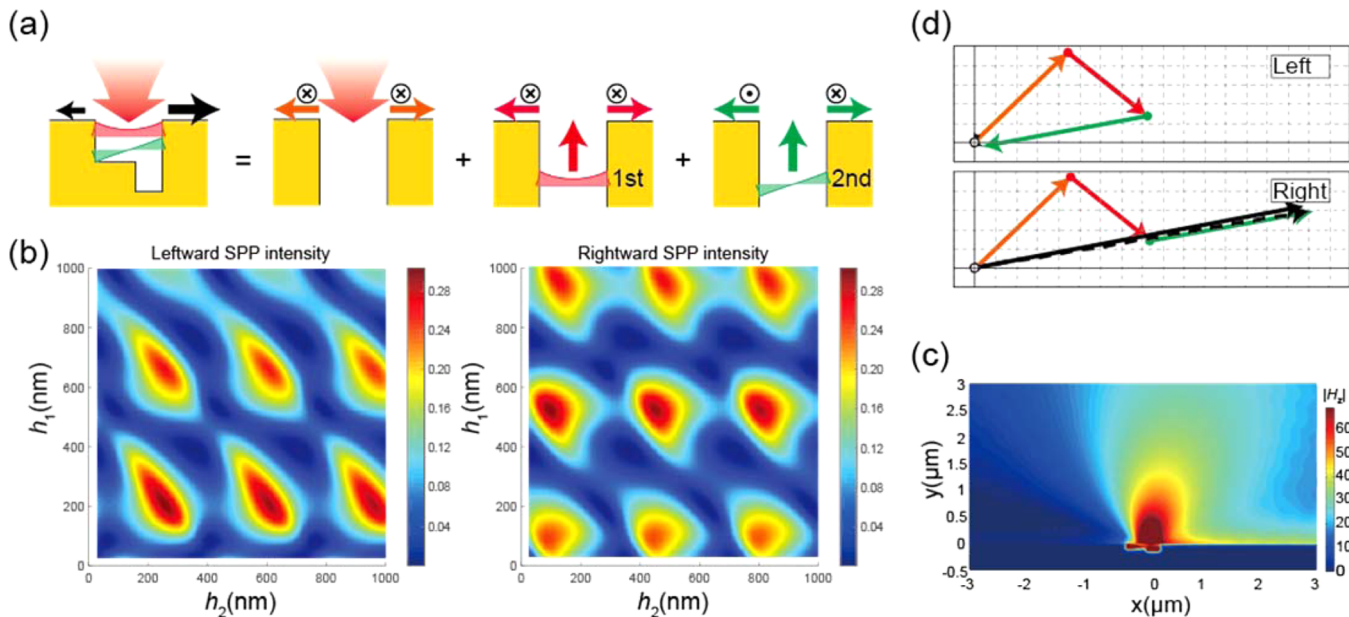


Figure 3. Directional excitation of SPPs by a single-element plasmonic nanoantenna with an auxiliary structure. (a) Three main origins of final SPPs on the front metal surface. These origins include SPPs excited at the entrance of the upper main groove by directly incident beam and upward propagating first and second modes. The cross in circle and dot in circle symbols represent the magnetic field is directed into and out of the plane of the figure, respectively. These symbols are engage to indicate the symmetry of different modes. (b) SPP intensities launched to the left and right directions by the proposed antenna structure in Figure 1b, at various h_1 and h_2 . (c) Simulated magnitude of scattered magnetic field under a specific geometry of $h_1 = 79$ nm and $h_2 = 52$ nm, with unidirectional launching of SPPs to the right clearly observed. (d) Corresponding vector diagrams displaying the three main SPP contributions to total SPPs. The meaning of each color vector is indicated on the front metal surface in panel a. All above calculations are performed at $\lambda = 800$ nm, $w_1 = 550$ nm, and $w_2 = 200$ nm.

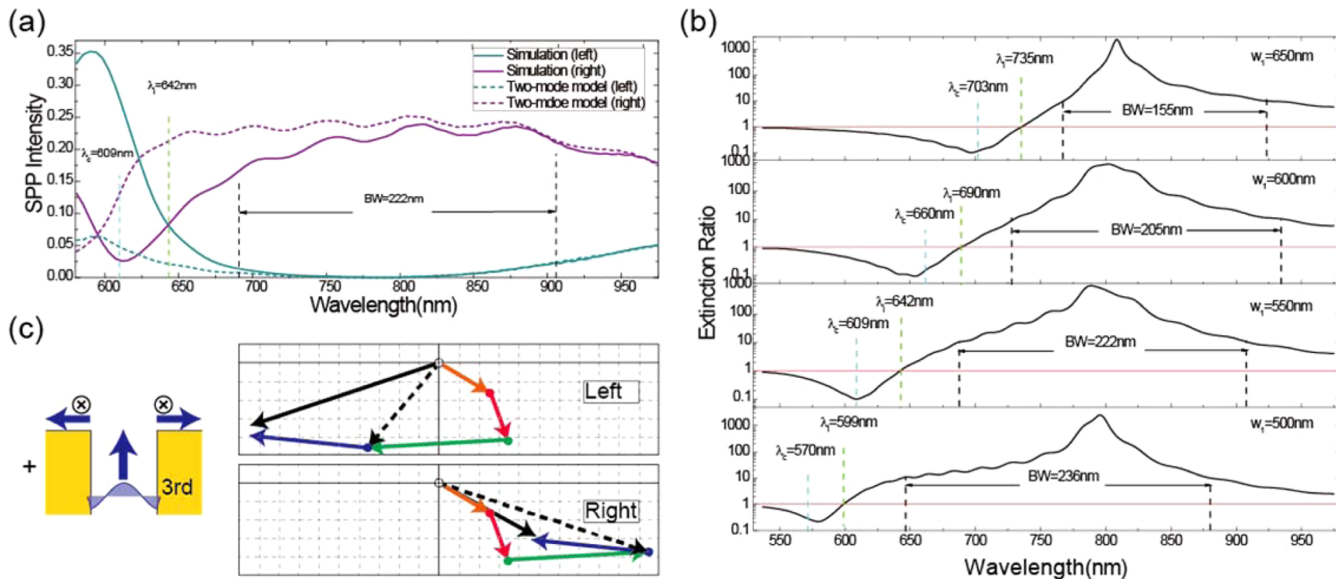


Figure 4. Wavelength response of directional SPP excitations by the proposed single-element plasmonic nanoantenna. (a) Simulated total SPP intensities (solid lines) to the left and right directions at various incident wavelengths and corresponding two-mode model results (dashed lines) that only take into account the SPP contributions from the directly incident beam and first and second modes in the main groove. (b) Simulated E_R spectra at $w_1 = 500, 550, 600$, and 650 nm. w_2 is fixed at 200 nm and h_1 and h_2 are adjusted to achieve the highest E_R at $\lambda = 800$ nm. The dashed lines indicate the critical wavelength λ_c at which $E_R = 1$ and the cutoff wavelength λ_c of the third mode in the main groove. (c) Vector diagrams showing different SPP contributions at $\lambda = 626$ nm. In addition to the three SPP contributions at $\lambda = 800$ nm in Figure 3d, the SPPs excited by the nonpropagating (or evanescent) third mode, which are represented by the blue vectors, play a significant role. The left inset provides a schematic explanation of this SPP component.

204 unidirectional SPP excitation to only one direction.¹⁸ In real
205 experiments, small groove depths are preferred because they are
206 easy to fabricate. Therefore, the smallest possible groove depths
207 of $h_1 = 79$ nm and $h_2 = 52$ nm are chosen in this study. Figure
208 3c shows the corresponding scattered field by the proposed
209 single-element nanoantenna. A nearly perfect directional
210 launching of SPPs to the right is clearly observed. The
211 extinction ratio E_R , which is defined as the rightward SPP
212 intensity over the leftward one, is $>10^3$. The specific
213 contributions of the three main SPP origins were evaluated
214 by calculating the three basic SPP excitation processes on the
215 right side of the “=” in Figure 3a one by one. The results are
216 intuitively indicated by vectors in Figure 3d with the vector
217 lengths and directions corresponding to the amplitudes and
218 phases of different SPP components (for more detailed
219 information on the vector diagram, see Section 4 in the
220 Supporting Information). The orange and red vectors,
221 respectively, correspond to the SPPs excited by the directly
222 incident beam and the upward symmetric first mode. Figure 3d
223 shows that both these two SPP contributions are in phase for
224 the left and right directions. On the contrary, the SPPs excited
225 by the antisymmetric second mode are in antiphase for the left
226 and right directions. Thus, these antiphase SPPs are
227 represented by two opposite green vectors in Figure 3d, one
228 vector denoting the left and the other denoting the right. The
229 green vector denoting the left just cancels the summation of the
230 orange and red vectors. This results in SPP extinction in this
231 direction. Meanwhile, the opposite green vector denoting the
232 right constructively interferes with the summation of the orange
233 and red vectors. This occurrence causes highly efficient
234 directional SPP launching to the right direction. The total
235 SPPs on the front metal surface are also directly evaluated and
236 indicated by the black solid vectors in Figure 3d. These vectors
237 agree well with the summation of the three color vectors which

are indicated by the black dashed vectors. In the figure, black
238 vectors representing the left direction are extremely short to be
239 seen because of the SPP extinction. Thus, the previous model
240 analysis and proposal for directional SPP excitation are well
241 confirmed, and the key role of effective excitation of the
242 antisymmetric second mode is clearly presented. Further
243 simulations show that up to 21% of the total incident power
244 can be launched into the rightward SPPs for a tightly focused
245 Gaussian incidence with a waist size of $w_0 = 480$ nm. This
246 absolute coupling efficiency is rather high, considering the
247 subwavelength lateral dimension of the proposed antenna
248 structure. For comparison, the efficiency of the antenna without
249 an auxiliary nanogroove reaches only 11%.
250

The above results are obtained with specific geometrical
251 parameters of $w_1 = 550$ nm and $w_2 = 200$ nm. More simulations
252 show that the main conclusions (i.e., efficient mode conversion
253 and directional SPP excitation) can be extended to more
254 general cases as long as the main groove supports only the first
255 and second modes and the auxiliary nanogroove supports only
256 the first mode.
257

Wavelength-dependent property is an important aspect for a
258 directional nanoantenna. The cyan and purple solid lines in
259 Figure 4a show simulated SPP intensities to the left and right
260 directions at various incident wavelengths (with $w_1 = 550$ nm,
261 $w_2 = 200$ nm, $h_1 = 79$ nm, and $h_2 = 52$ nm). Directional SPP
262 excitation clearly presents a broadband response around the
263 central wavelength of $\lambda = 800$ nm. The third panel in Figure 4b
264 shows the corresponding spectrum of the extinction ratio E_R .
265 Here, we define the bandwidth (BW) of a directional SPP
266 excitation as the wavelength range over which $E_R \geq 10$,
267 considering that such an E_R value is sufficient for enormous
268 unidirectional SPP couplers. For the current case, BW reaches
269 222 nm, which is a fairly satisfactory outcome. This broadband
270 response is mainly attributed to the shallow grooves used in the
271

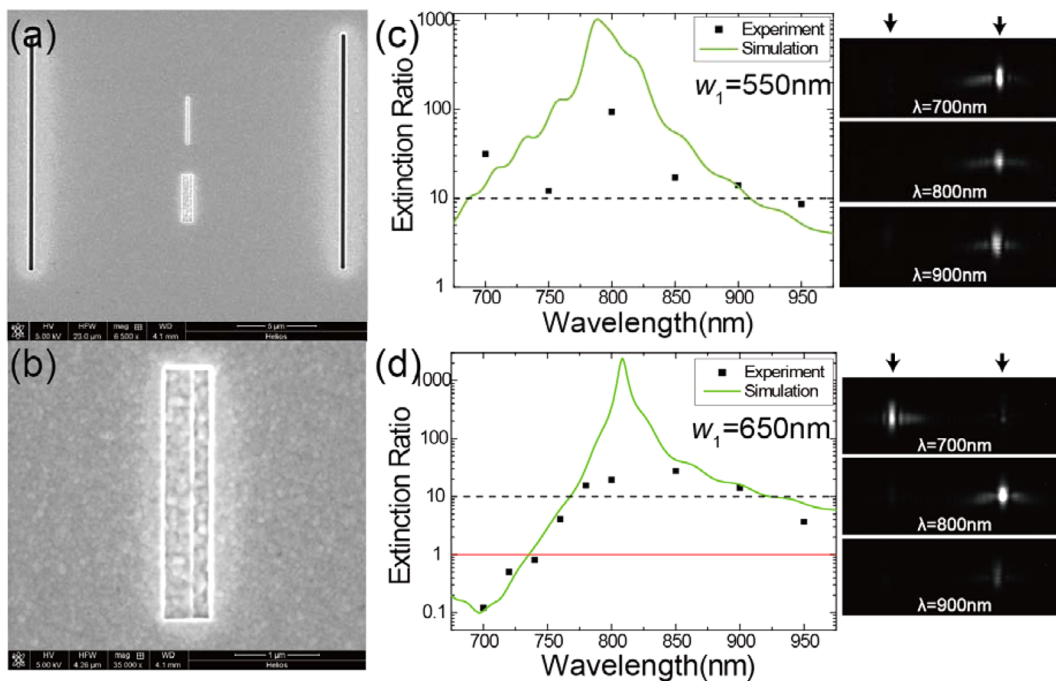


Figure 5. Experimental verification of directional SPP excitations using the proposed plasmonic nanoantenna. (a) SEM image of the structure of a sample. In the middle of the image, the proposed single-element nanoantenna is at the lower half, and a simple 100-nm-wide nanogroove at the upper half acts as an in-chip reference. Two observation slits that cut through the metal film and lie symmetrically on two sides of the central structure with a distance of 10 μm are designed to reconverge launched SPPs back into photons. (b) SEM image that shows a closer look of the proposed single-element nanoantenna with an auxiliary nanogroove. (c) Extinction ratio E_R at different wavelengths for sample 1 ($w_1 = 550\text{ nm}$, $h_1 = 79\text{ nm}$, $w_2 = 200\text{ nm}$, and $h_2 = 52\text{ nm}$), which presents the best broadband response of SPP directional excitation. (d) Extinction ratio E_R at different wavelengths for sample 2 ($w_1 = 650\text{ nm}$, $h_1 = 87\text{ nm}$, $w_2 = 200\text{ nm}$, and $h_2 = 33\text{ nm}$), which shows direction inversion of SPP excitation. The scatters are experimental results, and the green lines are simulation results. The right-side insets show typical CCD images, wherein directional SPP excitations are clearly observed (arrows indicate the locations of the two observation slits).

study. Small groove depths mean slow variations in the propagating phase factors of different modes when incident wavelength changes. Therefore, the resulting bandwidth is large. In contrast, BW decreases to 50 nm if another optimized geometry with deeper grooves of $h_1 = 550\text{ nm}$ and $h_2 = 440\text{ nm}$ are selected for achieving directional SPP excitation at $\lambda = 800\text{ nm}$.

Another interesting feature is the inversion of SPP launching direction at different wavelengths. In contrast to the slow variations in SPP intensities near the central wavelength of $\lambda = 800\text{ nm}$, SPP intensities change rapidly at the short-wavelength region, and the leftward SPP intensity rapidly exceeds the rightward intensity. A minimum E_R of 0.1 is obtained at $\lambda = 609\text{ nm}$. This value means that a highly directional SPP excitation to the left direction is achieved. Several E_R spectra at different w_1 are calculated to understand the underlying physical mechanism of SPP direction inversion. In the simulations, w_2 is fixed at 200 nm and h_1 and h_2 are adjusted to achieve the highest E_R at the same central wavelength of $\lambda = 800\text{ nm}$. The results are shown in different panels in Figure 4b. E_R remains high over a wide wavelength range near $\lambda = 800\text{ nm}$ in all the four panels, which indicates that broadband directional SPP excitations to the right direction occur. Meanwhile, all of the SPP excitation directions change to the left direction at short wavelengths. The inversion wavelength λ_i , which is defined as the critical wavelength at which $E_R = 1$, increases with w_1 . This phenomenon implies that the third-order (third) mode in the main groove may play a role because the cutoff wavelength λ_c of this mode also increases with w_1 (for the definition and evaluation of λ_c , see Section 1 in the Supporting Information). The dashed lines in

Figure 4b indicate the locations of λ_i and λ_c . Although λ_i and λ_c do not coincide with each other, a clear correlation is observed. To test the above hypothesis, we introduce the two-mode model that calculates the summation of SPP components contributed by the directly incident beam, first and second modes (for detailed information on the two-mode model, see Section 4 in the Supporting Information). Therefore, the discrepancy between the results of this model and the direct simulation results that naturally include SPP components contributed by all waveguide modes can intuitively indicate the SPP contributions from nonpropagating modes. The cyan and purple dashed lines in Figure 4a show the results of this model, which agree with direct simulation results in the long-wavelength region but deviates more and more toward the cutoff wavelength λ_c of the third mode. This phenomenon directly reflects the impact of the third mode. As a typical example, the vector diagrams in Figure 4c show the different SPP components at $\lambda = 626\text{ nm}$ (i.e., in the middle of λ_i and λ_c). Contrary to the results at $\lambda = 800\text{ nm}$ which are shown in Figure 3d, summations of the orange, red, and green vectors (i.e., results of the two-mode mode), which are indicated by the black dashed vectors, now significantly deviate from the actual total SPPs (black solid vectors). Only when the SPP contributions from the third mode are taken into account, the modified-model results can match the direct simulation results. The SPP contributions from the third mode are represented by the two blue vectors in Figure 4c. These two vectors point to the same direction because the third mode is a symmetric mode. The above results clearly validate the previous hypothesis on the role of the third mode at the short-

332 wavelength region. The total SPPs change the launching
 333 direction because of the SPP contribution of this high-order
 334 mode. Without the contribution of this mode, the previous
 335 two-mode model still gives a directional SPP excitation to the
 336 right direction.

337 One thing needs special attention is that λ_i is obviously larger
 338 than λ_c . This means that the third mode starts to play a
 339 significant role even when it is nonpropagating (namely, below
 340 cut off) or evanescent. The reason is that the groove is so
 341 shallow that even the exponentially decaying nonpropagating
 342 mode maintains a considerable intensity over such a
 343 subwavelength distance. That is why the SPPs contributed by
 344 the nonpropagating third mode are comparable to or even
 345 stronger than the SPPs contributed by the propagating second
 346 and first modes at $\lambda = 626$ nm, as shown in Figure 4c. The
 347 observed inversion of SPP launching direction indicates that the
 348 exploitation of nonpropagating modes may provide new
 349 possibilities to the design of nanoscale optical devices in
 350 addition to conventional propagating modes. However, this
 351 strategy is only applicable when the nonpropagating mode is
 352 not far below the cut off. Otherwise, the SPP contribution by
 353 this mode is negligible because of the significant propagation
 354 loss. That is why the third mode need not to be considered at λ
 355 = 800 nm, which is much larger than $\lambda_c = 609$ nm.

356 To validate our proposal experimentally, the sample
 357 structures were fabricated using direct focused ion beam
 358 (FIB) milling on a 450-nm-thick gold film that was evaporated
 359 on a glass substrate. Figure 5a shows a typical scanning electron
 360 microscope (SEM) image. Two 3- μm -long grooves are
 361 presented in the middle of the image. The lower groove is
 362 the proposed single-element plasmonic nanoantenna with an
 363 auxiliary nanogroove. Figure 5b provides a detailed image of
 364 this antenna. The upper groove is a simple 100-nm-wide
 365 nanogroove, which acts as an in-chip reference for sample
 366 alignment. Two nanoslits that cut through the metal film and
 367 lie symmetrically on the two sides of the central structure are
 368 designed to reconvert the launched SPPs back into photons.
 369 Thus, far-field detected signals provide a direct measurement of
 370 the relative intensities of evanescent SPPs.

371 The laser source is a Ti:sapphire laser, and its wavelength is
 372 tunable from 700 to 950 nm. In the measurement, the
 373 nanoantenna was normally illuminated from the front side
 374 using a p-polarized (electric field perpendicular to the groove)
 375 laser beam with a diameter of approximately 3 μm . A fraction of
 376 the launched SPPs that leak through the observation slits was
 377 collected using an objective from the substrate side and imaged
 378 onto a charge coupled device (CCD). Thus, the extinction ratio
 379 of the proposed antenna structure could be measured by
 380 comparing the signal intensities of the two observation slits.
 381 These signal intensities are evaluated by integrating over the
 382 detected light spots. The scatters in Figure 5c and d show the
 383 measured results at different incident wavelengths. Figure 5c
 384 displays the results obtained from sample 1 ($w_1 = 550$ nm, $h_1 =$
 385 79 nm, $w_2 = 200$ nm, and $h_2 = 52$ nm). This sample is chosen to
 386 present the best broadband response of SPP directional
 387 excitation in the measured spectral range from 700 to 950
 388 nm. The observed bandwidth that exhibits an $E_R \geq 10$ is larger
 389 than 200 nm. The insets in Figure 5c demonstrate the typical
 390 CCD images taken at $\lambda = 700$, 800, and 900 nm. These images
 391 clearly show the high contrast between the SPPs launched to
 392 the left and right directions. The measured maximum E_R
 393 reaches 94 at $\lambda = 800$ nm. Figure 5d displays the results
 394 obtained from sample 2 ($w_1 = 650$ nm, $h_1 = 87$ nm, $w_2 = 200$

395 nm, and $h_2 = 33$ nm). This sample is selected to demonstrate
 396 the direction inversion of SPP excitation. The insets in Figure
 397 5d show that the SPPs are primarily launched to the left
 398 direction at $\lambda = 700$ nm (left:right = 8:1) and the right direction
 399 at $\lambda = 800$ nm (left:right = 1:19). Direction inversion of SPP
 400 excitation is clearly observed. The measured spectra of E_R for
 401 both two samples consist with FEM simulation results (lines in
 402 Figure 5c and d). Only extinction ratios with extremely high
 403 values are not as high as the simulation results. This is
 404 understandable considering that the samples are not perfectly
 405 fabricated, and roughness of the sample decreases device
 406 performance. This deficiency may be overcome by using other
 407 fabrication techniques which provide decreased sample rough-
 408 ness, such as template stripping methods.³² Nevertheless, the
 409 measured high extinction ratio itself has already validated the
 410 theoretical prediction of directional SPP excitation.

In conclusion, this study demonstrates that highly efficient
 lowest-order mode can be effectively transferred into higher-
 order modes by adding an auxiliary resonant structure to the
 main structure of a single-element plasmonic nanoantenna.
 This mode conversion provides a novel degree of freedom to
 effectively excite higher-order antenna modes, which greatly
 facilitates further manipulations of scattered optical fields. As
 typical examples, both broadband directional excitation of SPPs
 and inversion of SPP launching direction at different wave-
 lengths are presented, which are unable to be obtained
 simultaneously in any previously reported structures. Although
 the current work is performed under the specific configuration
 of metallic groove antenna, the strategy of exploiting mode
 conversion and mode interference can be applied to various
 antenna structures, such as metallic nanostripe antennas,
 metallic slot antennas, metallic nanorod antennas, or even
 dielectric nanoantennas. Therefore, the proposed method based
 on mode conversion and mode interference provides new
 opportunities for the design of nanoscale optical devices,
 especially in the research area of directional nanoantennas.

■ ASSOCIATED CONTENT

● Supporting Information

Information on different waveguide modes, a semianalytical
 model describing the mode conversion and interference
 processes, comparison between the asymmetric slit and groove
 structures, and details on vector diagrams and the two-mode
 model. This material is available free of charge via the Internet
 at <http://pubs.acs.org>.

■ AUTHOR INFORMATION

Corresponding Authors

*E-mail: HMLiao@pku.edu.cn

*E-mail: z_li@pku.edu.cn.

Author Contributions

§W. Y. and S. L. contributed equally to the work.

Notes

The authors declare no competing financial interest.

■ ACKNOWLEDGMENTS

This work was supported by the National Basic Research
 Program of China (Grant No. 2013CB328704) and the
 National Natural Science Foundation of China (Grant Nos.
 61475002 and 61435001).

REFERENCES

- 452 (1) Lal, S.; Link, S.; Halas, N. J. *Nat. Photonics* **2007**, *1*, 641–648.
- 453 (2) *Nano-Optics and Near-Field Optical Microscopy*; Zayats, A. V.,
454 Richards, D., Eds.; Artech House: Boston, 2009.
- 455 (3) Schuller, J. A.; Barnard, E. S.; Cai, W. S.; Jun, Y. C.; White, J. S.;
456 Brongersma, M. L. *Nat. Mater.* **2010**, *9*, 193–204.
- 457 (4) Bozhevolnyi, S. I.; Volkov, V. S.; Devaux, E.; Laluet, J.-Y.;
458 Ebbesen, T. W. *Nature* **2006**, *440*, 508–511.
- 459 (5) Mühlischlegel, P.; Eisler, H.-J.; Martin, O. J. F.; Hecht, B.; Pohl, D.
460 W. *Science* **2005**, *308*, 1607–1609.
- 461 (6) Kosako, T.; Kadoya, Y.; Hofmann, H. F. *Nat. Photon* **2010**, *4*,
462 312–315.
- 463 (7) Curto, A. G.; Volpe, G.; Tamini, T. H.; Kreuzer, M. P.;
464 Quidant, R.; van Hulst, N. F. *Science* **2010**, *329*, 930–933.
- 465 (8) Noginov, M. A.; Zhu, G.; Belgrave, A. M.; Bakker, R.; Shalaev, V.
466 M.; Narimanov, E. E.; Stout, S.; Herz, E.; Suteewong, T.; Wiesner, U.
467 *Nature* **2009**, *460*, 1110–1112.
- 468 (9) Oulton, R. F.; Sorger, V. J.; Zentgraf, T.; Ma, R. M.; Gladden, C.;
469 Dai, L.; Bartal, G.; Zhang, X. *Nature* **2009**, *461*, 629–632.
- 470 (10) Rolly, B.; Stout, B.; Bonod, N. *Opt. Express* **2012**, *20*, 20376–
471 20386.
- 472 (11) Fu, Y. H.; Kuznetsov, A. I.; Miroshnichenko, A. E.; Yu, Y. F.;
473 Luk'yanchuk, B. *Nat. Commun.* **2013**, *4*, 1527.
- 474 (12) Vercruyse, D.; Sonnenfraud, Y.; Verellen, N.; Fuchs, F. B.; Di
475 Martino, G.; Lagae, L.; Moshchalkov, V. V.; Maier, S. A.; Van Dorpe,
476 P. *Nano Lett.* **2013**, *13*, 3843–3849.
- 477 (13) Hancu, I. M.; Curto, A. G.; Castro-López, M.; Kuttge, M.; van
478 Hulst, N. F. *Nano Lett.* **2014**, *14*, 166–171.
- 479 (14) Coenen, T.; Arango, F. B.; Koenderink, A. F.; Polman, A. *Nat.
480 Commun.* **2014**, *5*, 3250.
- 481 (15) Panaro, S.; Nazir, A.; Liberale, C.; Das, G.; Wang, H.; De
482 Angelis, F.; Zaccaria, R. P.; Di Fabrizio, E.; Toma, A. *ACS Photonics*
483 **2014**, *1*, 310–314.
- 484 (16) Pan, D.; Wei, H.; Jia, Z. L.; Xu, H. X. *Sci. Rep.* **2014**, *4*, 4993
485 DOI: 10.1038/srep04993.
- 486 (17) López-Tejeira, F.; Rodrigo, S. G.; Martín-Moreno, L.; García-
487 Vidal, F. J.; Devaux, E.; Ebbesen, T. W.; Krenn, J. R.; Radko, I. P.;
488 Bozhevolnyi, S. I.; González, M. U.; Weeber, J. C.; Dereux, A. *Nat.
489 Phys.* **2007**, *3*, 324–328.
- 490 (18) Chen, J. J.; Li, Z.; Yue, S.; Gong, Q. H. *Appl. Phys. Lett.* **2010**,
491 97, 041113.
- 492 (19) Baron, A.; Devaux, E.; Rodier, J.-C.; Hugonin, J.-P.; Rousseau,
493 E.; Genet, C.; Ebbesen, T. W.; Lalanne, P. *Nano Lett.* **2011**, *11*, 4207–
494 4212.
- 495 (20) Liu, J. S. Q.; Pala, R. A.; Afshinmanesh, F.; Cai, W. S.;
496 Brongersma, M. L. *Nat. Commun.* **2011**, *2*, 525.
- 497 (21) Liu, Y.; Palomba, S.; Park, Y.; Zentgraf, T.; Yin, X.; Zhang, X.
498 *Nano Lett.* **2012**, *12*, 4853–4858.
- 499 (22) Rodríguez-Fortuño, F. J.; Marino, G.; Ginzburg, P.; O'Connor,
500 D.; Martínez, A.; Wurtz, G. A.; Zayats, A. V. *Science* **2013**, *340*, 328–
501 330.
- 502 (23) Lin, J.; Mueller, J. P. B.; Wang, Q.; Yuan, G.; Antoniou, N.;
503 Yuan, X.-C.; Capasso, F. *Science* **2013**, *340*, 331–334.
- 504 (24) Liao, H. M.; Li, Z.; Chen, J. J.; Zhang, X.; Yue, S.; Gong, Q. H.
505 *Sci. Rep.* **2013**, *3*, 1918 DOI: 10.1038/srep01918.
- 506 (25) Lalanne, P.; Hugonin, J. P.; Rodier, J. C. *Phys. Rev. Lett.* **2005**,
507 95, 263902.
- 508 (26) Lalanne, P.; Hugonin, J. P.; Rodier, J. C. *J. Opt. Soc. Am. A* **2006**,
509 23, 1608–1615.
- 510 (27) Raghunathan, S. B.; Gan, C. H.; van Dijk, T.; Kim, B. E.;
511 Schouten, H. F.; Ubachs, W.; Lalanne, P.; Visser, T. D. *Opt. Express*
512 **2012**, *20*, 15326–15335.
- 513 (28) Raghunathan, S. B.; Schouten, H. F.; Ubachs, W.; Kim, B. E.;
514 Gan, C. H.; Visser, T. D. *Phys. Rev. Lett.* **2013**, *111*, 153901.
- 515 (29) Johnson, P. B.; Christy, R. W. *Phys. Rev. B* **1972**, *6*, 4370–4379.
- 516 (30) Snyder, A. W.; Love, J. D. *Optical Waveguide Theory*; Chapman
517 and Hall: New York, 1983.
- 518 (31) Lalanne, P.; Hugonin, J. P.; Liu, H. T.; Wang, B. *Surf. Sci. Rep.*
519 **2009**, *64*, 453–469.
- 520